Spectroscopic reverberation mapping of Quasar PKS 0736 + 017: broad-line region and black-hole mass

Shivangi Pandey,[1]⋆ Suvendu Rakshit ®,[1]⋆ Jong-Hak Woo[2] and C. S. Stalin ®[3]

[1]*Aryabhatta Research Institute of Observational Sciences, Nainital-263001, Uttarakhand, India*
[2]*Astronomy Program, Department of Physics and Astronomy, Seoul National University, Seoul, 08826, Republic of Korea*
[3]*Indian Institute of Astrophysics, Block II, Koramangala, Bangalore-560034, India*

ABSTRACT

To understand the mass distribution and co-evolution of supermassive black holes with their host galaxy, it is crucial to measure the black hole mass of AGN. Reverberation mapping is a unique tool to estimate the black hole masses in AGN. We performed spectroscopic reverberation study using long-term monitoring data with more than 100 spectra of a radio-loud quasar PKS 0736 + 017 to estimate the size of the broad-line region (BLR) and black hole mass. The optical spectrum shows strong $H\beta$ and $H\gamma$ emission lines. We generated the light curves of 5100 Å continuum flux (f_{5100}), $H\beta$, and $H\gamma$. All the light curves are found to be strongly variable with fractional variability of 69 per cent, 21 per cent, 30 per cent for V-band, $H\beta$, and $H\gamma$ light curves, respectively. Along with the thermal contribution, non-thermal emission contributes to the estimated continuum luminosity at 5100 Å. Using different methods, e.g. CCF, JAVELIN, von-neumann, we estimated the size of the BLR, which is found to be $66.4^{+6.0}_{-4.2}$ light days in the rest frame. The BLR size combined with the line width of $H\beta$ provides a black hole mass of $7.32^{+0.89}_{-0.91} \times 10^7 M_\odot$. The source closely follows the BLR size–luminosity relation of AGN.

Key words: techniques: spectroscopic – galaxies: active – galaxies: individual: PKS0736 + 017.

1 INTRODUCTION

Active galactic nuclei (AGNs) are powered by the accretion of matter on to a central supermassive black hole (SMBH) of mass M > 10^6 M$_\odot$ (Woo & Urry 2002). These are one of the most bright and persistent objects in the Universe ($\gtrsim 10^{44}$ ergs s^{-1}), which outshine their entire host galaxy by emitting an abundant amount of radiation in a broad range of the electromagnetic region. It shows flux variation over a time-scale of months to years (e.g. Wagner & Witzel 1995; Ulrich, Maraschi & Urry 1997). The emission from AGN peaks at the UV/optical region of the spectral energy distribution (SED). Due to the strong gravity of a black hole, matter attracted toward it spirals in and forms a disc-like structure known as an accretion disc. Surrounding this is the broad-line region (BLR), which is made of gas clouds orbiting around the SMBH with velocities of a few thousand km s^{-1}. The gas is ionized by the continuum radiation and emits broad emission lines due to Doppler broadening (Urry & Padovani 1995).

The black hole mass is strongly correlated with the host galaxy properties suggesting a co-evolution of black hole and host galaxy (Kormendy & Ho 2013) and subsequently studying these AGNs provides leverage to probe the growth and evolution of black holes and their host galaxy across the Universe. The mass of the black hole in AGN is challenging to measure because the bright central core overpowers the host galaxy, and the spatial resolution needed to resolve the central structure is beyond the capability of existing telescopes (however, see Gravity Collaboration 2018;

GRAVITY Collaboration 2020). The black hole mass measurement of a radio-loud object is more difficult due to the non-thermal contribution from jet, which affects the optical continuum variation of AGN.

Reverberation Mapping (RM; Blandford et al. 1982; Peterson 1993) uses the flux variability to estimate black hole masses and constrain the geometry and kinematics of the central engine. RM is based on the variation of line fluxes due to the variation of optical/UV photons from the accretion disc. RM is a well-known technique that has been applied so far in more than 100 objects to provide the BLR size and black hole mass (e.g. Bahcall et al. 1972; Blandford et al. 1982; Peterson 1993; Peterson et al. 1998; Wandel, Peterson & Malkan 1999; Kaspi et al. 2000, 2007; Peterson et al. 2002, 2004, 2014; Greene & Ho 2005; Bentz et al. 2009, 2010; Dietrich et al. 2012; Zu et al. 2013; Du et al. 2014, 2015, 2016a, b, 2018; Barth et al. 2015; Woo et al. 2015; Shen et al. 2016; Fausnaugh et al. 2017; Grier et al. 2017; Park et al. 2017; Pei et al. 2017; Rakshit et al. 2019; Zhang et al. 2019; Bontà et al. 2020; Cho et al. 2020; Rakshit 2020; Williams et al. 2020; Amorim et al. 2021; Cackett, Bentz & Kara 2021; Dehghanian et al. 2021; Bentz, Williams & Treu 2022; Villafaña et al. 2022; U et al. 2022). Remarkably, it has provided a relation between $H\beta$ BLR size and luminosity at 5100 Å (L_{5100}) that can be used to estimate BLR size and black hole mass of any AGN having a single-epoch spectrum (Bentz et al. 2013). RM study of high-accreting sources (Du et al. 2016a, b, 2018) show significant deviation from the BLR size–luminosity relation, which is found due to Eddington ratio/Fe II strength (Du & Wang 2019). Therefore, proper calibration of the size–luminosity relation is crucial by increasing the sample size and objects with diverse properties. Moreover, emission-line and

⋆ E-mail: shivangi101096@gmail.com (SP); Suvenduat@gmail.com (SR)

continuum light curves can be used to estimate the BLR size and constrain the geometry and kinematics of the BLR via geometrical and dynamical models (e.g. Pancoast et al. 2014; Mandal et al. 2020).

RM of radio-loud AGN is challenging due to the contribution of non-thermal emission, as a consequence, RM has been successfully performed only for a few radio-loud AGNs. For example, H β lag of 3C 120 and 3C 273 has been well-measured by Peterson et al. (1998) and Kaspi et al. (2000), respectively (see also Zhang et al. 2019, for 3c273). Rakshit (2020) successfully measured H β lag of PKS1510-089. RM study based on Mg II line of radio-loud AGN has also been carried out successfully for HE 0413-4031 by Zajaček et al. (2020); however, in some cases strong non-thermal contribution prevented reliable lag measurement (e.g. Nalewajko et al. 2019; Chavushyan et al. 2020; Amaya-Almazán, Chavushyan & Patiño-Álvarez 2022).

PKS 0736 + 017 (hereafter PKS0736) is a flat-spectrum radio quasar (FSRQ) located at the redshift of 0.189 (Lynds 1967; Tadhunter et al. 1993). The SED of PKS0736 spans from the radio through the γ-ray wavelengths, consisting of the typical double hump structure of Blazars where the low-energy hump is due to synchrotron emission and high-energy one is due to the external Compton process (Impey & Neugebauer 1988; Fossati et al. 1998; Clements, Jenks & Torres 2003; Abdalla et al. 2020). The source shows a one-sided parsec-scale jet (Kellermann et al. 1998; Bloom et al. 2009) and a compact core (Gower et al. 1984; Romney et al. 1984), and is speculated to have been hosted by an elliptical galaxy (Wright, McHardy & Abraham 1998; McLure et al. 1999; Falomo & Ulrich 2000). The optical-UV spectrum is characterized by broad emission lines and a big blue bump that is associated with thermal emission from the accretion disc (Baldwin 1975; Malkan & Moore 1986). The previous estimates of the black hole mass of PKS0736 based on the BLR size–luminosity relation elucidates 10^8–$10^{8.73}$ M$_\odot$ (Wandel et al. 1999; McLure & Dunlop 2001; Marchesini, Celotti & Ferrarese 2004; Dai et al. 2007; Abdalla et al. 2020). Therefore, the black hole mass of PKS0736 remains highly uncertain, and accurate measurement of the black hole mass will help SED modelling. Moreover, the BLR of PKS0736 is poorly studied due to the unavailability of long-duration spectroscopic monitoring.

In this paper, we performed a spectroscopic variability study of PKS0736 to estimate the size of the BLR and black hole mass through RM. The optical data is taken from the Steward Observatory (SO) as a part of the spectropolarimetric monitoring project,[1] which is a support program for the *Fermi Gamma-Ray Space Telescope*. Apart from the 3C 273 reported by Zhang et al. (2019) and PKS 1510-089 reported by Rakshit (2020), PKS0736 have good-quality data with more than 100 spectra suitable for RM based on H β emission line. The optical spectrum shows a blue continuum and the presence of strong Balmer lines (H β and H γ) and Fe II emission. We performed several methods to calculate the size of the BLR and the black hole mass of PKS0736 from time-series analysis. In Section 2, we describe the data analysis, and in Section 3, we present the results of the spectral analysis and time-lag measurements using various methods. Subsequently, in Section 4, we discuss the results and conclude in Section 5.

2 DATA

2.1 Optical data

Spectroscopic monitoring of PKS0736 was performed in SO as a part of spectropolarimetric monitoring project (Smith et al. 2009), which is a support program for the *Fermi Gamma-Ray Space Telescope*. Observations were carried out using the 2.3m Bok Telescope on Kitt Peak and the 1.54m Kuiper Telescope on Mount Bigelow in Arizona using the spectrophotometric instrument SPOL (Schmidt, Stockman & Smith 1992) with a 600 mm^{-1} grating, which provides the spectral range of 4000–7550Å with a dispersion of 4 Å/pixel. Depending on the width of the slit used for the observation, the resolution is typically between 16 and 24 Å. Details regarding observations and data reduction are given in Smith et al. (2009). In short, differential photometry using a standard field star was performed to calibrate photometric magnitudes. The instrumental magnitudes of the AGN and the comparison star are determined by using a synthetic Johnson V bandpass for spectroscopic data. A total of 133 V-band photometric observations carried out between November 2014 and May 2018 were used. Spectra were flux-calibrated using the average sensitivity function derived from multiple observations of several spectrophotometric standard stars throughout an observing campaign. Final flux calibrations were performed, re-scaling the spectrum from a given night to match the synthetic V-band photometry of that night (see Smith et al. 2009). Therefore, a total of 127 photometrically calibrated spectra obtained between 2014 November and 2018 May were downloaded from the SO data base and used in this work. Among the 127 spectra, 107 spectra were observed with a slit width of 4.1 arcsec.

2.2 γ-ray and radio data

The γ-ray data within the energy range of 100MeV to 300GeV were collected from the publicly available data base of the *Large Area Telescope* (LAT) onboard the *Fermi Gamma-Ray Space Telescope* (Abdo et al. 2009) between 2014 December and 2017 November. The weekly binned reduced light curve was downloaded and used without any further processing from the light-curve Repository of LAT[2] (Fermi Large Area Telescope Collaboration 2021).

The 15GHz radio data observed using the 40m Telescope at the Owens Valley Radio Observatory (OVRO[3]) were also collected (Richards et al. 2011).

3 RESULTS AND ANALYSIS

3.1 Optical spectral analysis and light curves

First, the spectra are brought to the rest frame, then emission line fluxes are measured. Two methods are usually adopted in previous studies for flux measurement: (1) direct integration of emission lines within a given window after subtracting the power-law continuum (e.g. Kaspi et al. 2000; Grier et al. 2012; Fausnaugh et al. 2017; Du et al. 2018) and (2) detailed multicomponent spectral decomposition (e.g. Barth et al. 2015; Rakshit et al. 2019) that also isolate Fe II emission. However, the latter method demands high-S/N spectra, while the former works well even with moderate-low-S/N spectra. Both methods are found to provide consistent lag estimates (Du et al.

---

[1] http://james.as.arizona.edu/~psmith/Fermi/

[2] https://fermi.gsfc.nasa.gov/ssc/data/access/lat/LightCurveRepository/source.html?source_name = 4FGL_J0739.2 + 0137
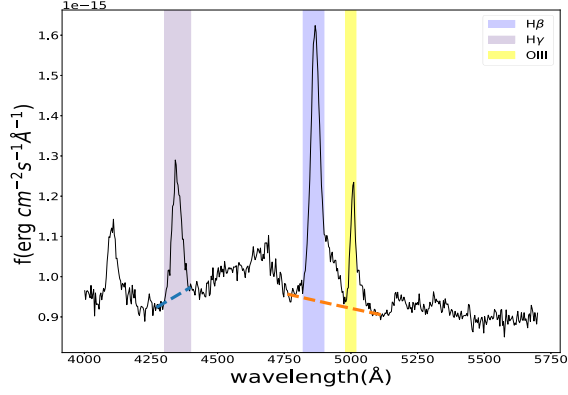[3] https://sites.astro.caltech.edu/ovroblazars/

Figure 1. Optical spectrum of PKS0736 on MJD = 57046.28, showing the presence of several emission lines. The shaded region represents the line integration windows, and the dashed lines show the best-fitting continuum.

Table 1. Emission-line region enlisted to calculate their respective flux.

Line	Wavelength range (Å)
H γ	4300–4400
Fe II	4435–4685
H β	4820–4900
O III	4980–5020

2016a). Here, we adopted the direct integration method due to its better robustness and applicability to the moderate S/N spectra like the one used in this work.

To calculate the emission line flux, we have fitted a power-law i.e. P(λ) $= \alpha \lambda^{\beta}$, where α is a normalization constant and β is the spectral index, locally for H β plus [O III] region in the wavelength window 4760–4790 and 5080–5120 Å, and separately for H γ region in the wavelength window of 4270–4290 and 4400–4405 Å as shown in Fig. 1. Then, we subtracted the best-fitting power-law model from each spectrum for both regions separately. Then using the power-law subtracted spectrum, we have integrated the flux values of each emission line region within given wavelength windows as mentioned in Table 1. It provides us with the flux for each line in each respective spectrum. Note that we consider the region 4820–4900 Å to calculate H β line flux because beyond 4900 Å there is an excess contribution from the Fe II 4924 Å multiplets and [O III]4959. This eventually creates a red asymmetry in the line profile of H β (see e.g. Joly 1988). Since the Fe II emission is also variable in AGNs, it will also be present in the RMS spectrum and hinder the calculation of width of the line emission of H β.

We have generated the light curves using the integrated flux values and the photometric V-band light curve obtained from SO. Using the best-fitting power-law used for H β and the [O III] region, we have calculated the continuum flux at 5100 Å. As mentioned in the previous section, the flux calibration of SO spectra is performed using standard stars observed throughout the campaign; therefore, seeing effect, slit loss, and systematic uncertainty contributes to the high uncertainty in the flux calibration. Hence, we rescaled the flux values based on the [O III] λ5007 emission lines considering it non-variable during the time-scale of the monitoring program. The final light curves are shown in Fig. 2. Uncertainties in the calculated emission line flux and continuum flux include systematic uncertainty and Poisson noise added in quadrature. The systematic uncertainties are estimated by the median filter method as described in Zhang et al. (2019), first, smoothing the light curve by a median filter with

five points and then subtracting the smoothed light curve from the original one. The standard deviation of the residual is used as the estimate of the systematic uncertainty. The flux values are provided in Table 2.

3.2 Variability

To quantify the variability amplitude of the light curves, we estimated the fractional variability amplitude (F_{var}) for V-band, f_{5100}, H β, and H γ light curves using the following equation (Rodriguez-Pascual et al. 1997).

$$F_{\mathrm{var}} = \frac{\sqrt{(\sigma^2 - < \sigma^2_{\mathrm{err}} >)}}{< f >} \qquad (1)$$

where σ^2 is the variance, σ^2_{err} is the mean square error, and $<f>$ is the arithmetic mean of the light curves. The ratio of maximum to minimum flux variation (R_{max}) was also calculated for photometric and spectroscopic light curves. The values are given in Table 3. All the continuum and line light curves show significant variations with $F_{\mathrm{var}} = 21$ per cent for H β and 30 per cent for H γ. The R_{max} is found 3 and 5 for H β and H γ, respectively. The higher variability found in H γ compared to H β agrees well with the previous finding in the literature (see Bentz et al. 2010; Zhang et al. 2019) and as predicated from photo-ionization calculation (Korista & Goad 2004).

Between MJD = 57000–57285, the γ- ray flux is in an active or flaring state, and the same is reflected in the optical flux showing correlated variation. It suggests a strong non-thermal contribution from the jet dominates this part of the light curve. Although the same effect is not visible in the emission line fluxes. Considering the source is FSRQ, a non-thermal contribution from the jet to the optical flux is expected. To determine the dominance of non-thermal contribution over the thermal emission from the accretion disc, we calculated the non-thermal dominance (NTD; Shaw et al. 2012) using

$$\mathrm{NTD} = \frac{L_o}{L_p} \quad \mathrm{and} \quad L_o = L_{\mathrm{disc}} + L_{\mathrm{jet}} \qquad (2)$$

where L_o is the observed continuum luminosity having a combination of luminosity emitted from the accretion disc (L_{disc}) and the jet (L_{jet}). The L_p is the predicted disc continuum luminosity that can be assumed to be responsible for line luminosity coming out from the BLR. Therefore, if the thermal emission from the disc only ionizes the broad-line clouds and no effect of non-thermal emission is present for the same, then, $L_p = L_{\mathrm{disc}}$ and NTD will equalize to $1 + L_{\mathrm{jet}}$ /L_{disc}. If only thermal contribution from the disc is responsible for continuum luminosity, NTD becomes unity. NTD can be larger than 2 if the jet contribution is greater than the disc contribution.

To measure L_p, we used the correlation of $L_{\mathrm{H}\beta}$-$L_{5100\text{Å}}$ obtained by Rakshit, Stalin & Kotilainen (2020) for SDSS DR14 quasars and the $L_{\mathrm{H}\beta}$ estimated in this work via log $L_{\mathrm{H}\beta} = (1.057 \pm 0.002)$log $L_{5100\text{Å}}$ $+ (- 4.41 \pm 0.10)$. The variation of NTD with time is shown in the last panel of Fig. 2. We note the following points: (1) The NTD varies between 1.1 and 11.2 with an average of 2.7, suggesting that the non-thermal emission from the jet contributes to the continuum variation, and (2) from MJD = 57000–57285; the NTD shows strong spikes, which are correlated with the flaring event in the γ-ray light curve, increasing up to NTD = 11.

The correlation between the continuum and emission-line luminosity of PKS0736 is studied. In Fig. 3, H β luminosity (upper panel), γ-ray (middle), and NTD (bottom panel) are plotted against 5100 Å continuum luminosity. The NTD is larger than 2 when log $L_{5100} >$ 44.6 erg s^{-1}. Therefore, a significant non-thermal contribution in the optical emission is found above this luminosity and disc contribution
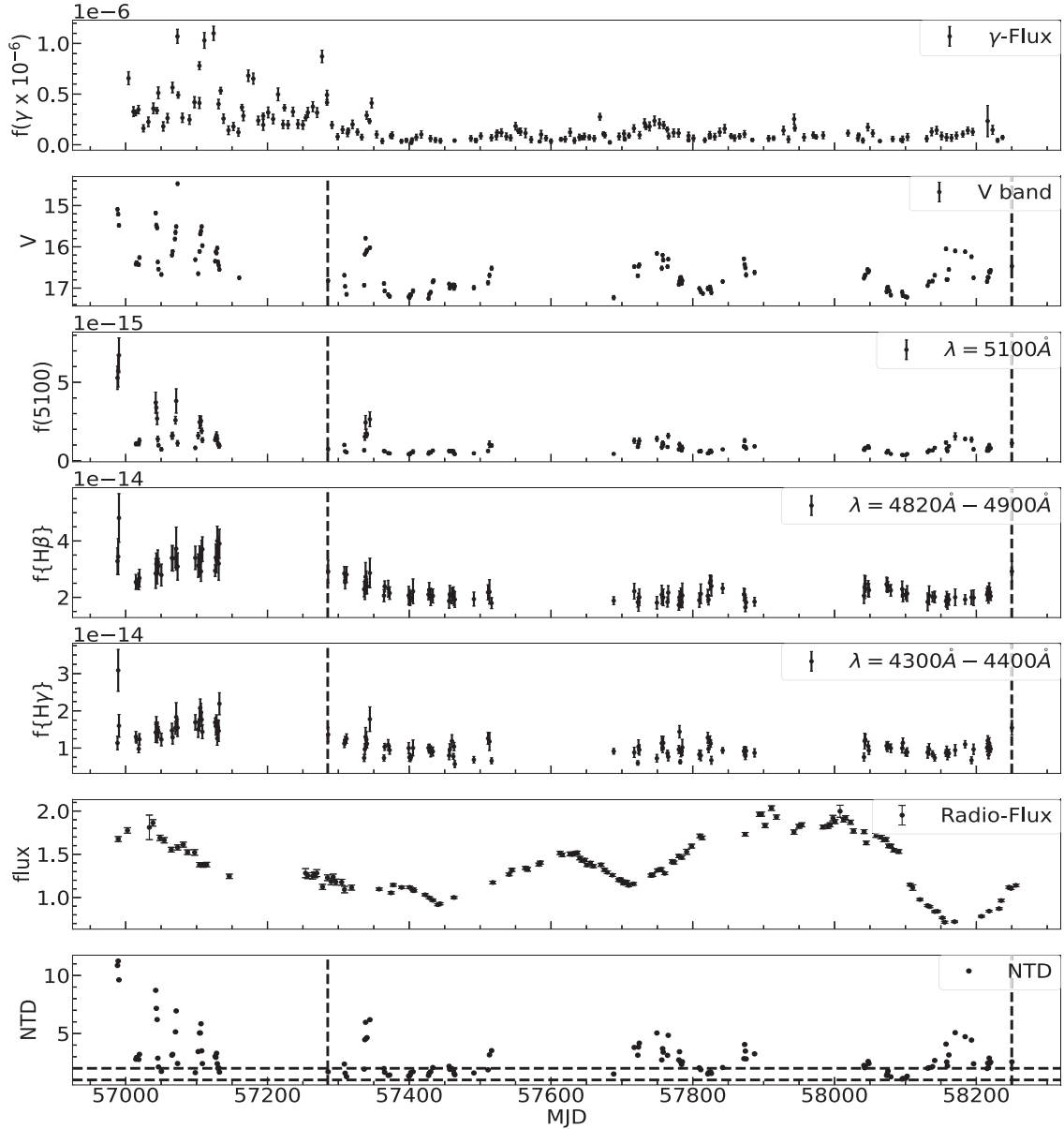
Figure 2. Light curves of PKS0736. Top to bottom: γ ray flux in photons s^{-1} cm^{-2}, photometric V-band magnitude, spectroscopic flux at 5100 Å in ergs cm^{-2}s^{-1} Å^{-1}, Hβ and Hγ flux in ergs cm^{-2}s^{-1}, radio flux in Jansky(Jy), NTD parameter. The vertical line at 57285 and 58250 is the MJD range that is used for time analysis, and horizontal lines represent NTD = 1 and 2.

Table 2. Columns as: (1) Modified Julian date (MJD), (2) photometric V-band magnitude, (3) spectroscopic flux at 5100 Å in units of 10^{-15} ergs cm^{-2} s^{-1} Å^{-1}, (4) and (5) are Hβ and Hγ line flux in units of 10^{-15} ergs cm^{-2}s^{-1}, respectively. This table is available in its entirety in machine-readable form. A portion is shown here for guidance.

MJD	V	f(5100)	f(Hβ)	f(Hγ)
(1)	(2)	(3)	(4)	(5)
56989	15.09	5.28 ± 0.59	29.15 ± 3.20	13.63 ± 1.62
56990	15.21	5.71 ± 0.49	28.45 ± 4.14	11.22 ± 1.63
56991	15.48	6.72 ± 1.18	25.32 ± 2.64	15.98 ± 2.95
57015	16.42	1.06 ± 0.12	28.09 ± 4.19	13.05 ± 1.55

Table 3. Variability statistics.

light curve	Median flux	F_{var} (%)	R_{max}
(1)	(2)	(3)	(4)
V-band	0.76 ± 0.07	69.86 ± 4.30	12.94 ± 0.67
f_{5100}	0.82 ± 0.11	85.43 ± 5.57	18.87 ± 4.11
Hβ	21.95 ± 0.66	21.10 ± 1.79	2.92 ± 0.63
Hγ	10.11 ± 0.41	29.73 ± 2.25	5.41 ± 0.88

Columns are: (1) light curve and (2) median flux of the light curve in units of 10^{-15} ergs s^{-1}cm^{-2} Å^{-1} for f_{5100}, and 10^{-15} ergs s^{-1}cm^{-2} for emission lines; (3) fractional rms variability in percentage; and (4) the ratio of maximum-to-minimum flux variation.
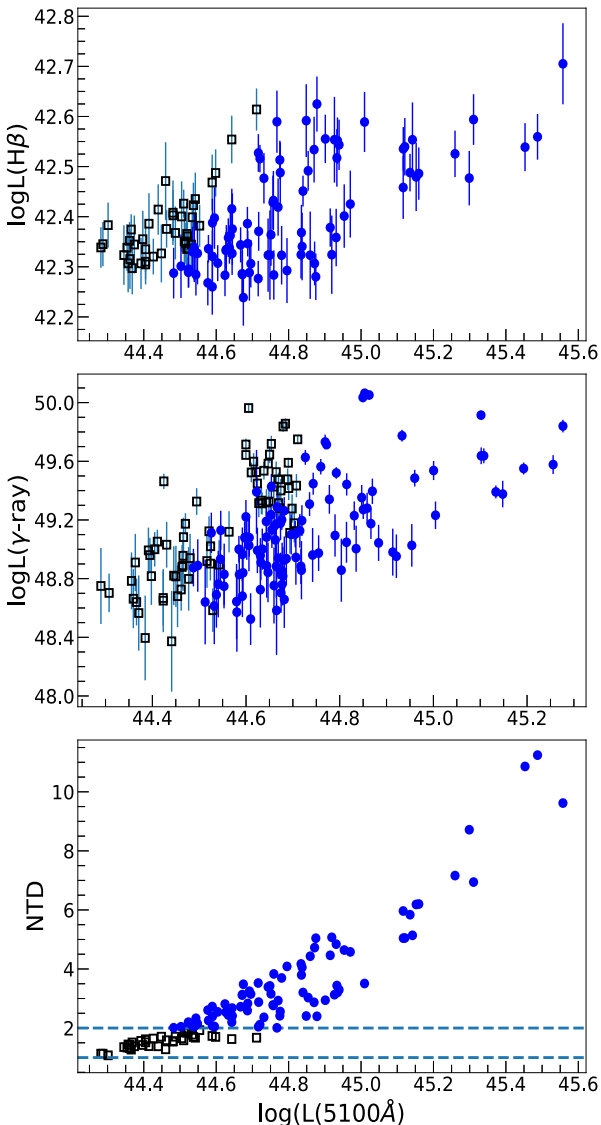
Figure 3. Top to bottom: plots shown are log L(Hβ), log L(γ), and NTD parameter against log L_{5100}. The black empty square represents data points with NTD < 2 while the filled blue circles are for NTD $\geq$ 2. The dotted horizontal lines are at NTD = 1 and 2.

found to dominate below this range. This is also clear from the correlation of line and continuum luminosity plot, which shows a large scatter above log $L_{5100} > 44.6$ erg s^{-1} (see upper panel of Fig. 3). The Spearman correlation coefficient calculated for $L_{H\beta}$ versus L_{5100} is noted as $r_s = 0.61$ with a p-value of no correlation to be $p = 10^{-15}$, whereas a much stronger and positive correlation is seen for data points where NTD < 2 with $r_s = 0.71$ and $p = 10^{-7}$. As shown in the Fig. 2, the γ-ray flux changes by a factor of 20 between MJD = 57000 and 57285 with the peak flux of 1.1×10^{-7} photons s^{-1} cm^{-2} on MJD = 57124.0. Apart from the flaring event during MJD = 57000–57285, the light curve is mostly quiescent. The F_{var} is found to be 99.5 per cent for full light curve and 51 per cent for MJD > 57285. Therefore, the variations in γ-ray is much larger than the optical flux variation. Optical continuum flux is found to be correlated with the γ-ray flux, with $r_s = 0.79$ and $p = 10^{-15}$ (see Fig. 3).

3.3 Time delay measurement

As mentioned in the previous section, a strong flare in the γ-ray light curves is seen between 57000 and 57285 MJD due to the dominance of non-thermal contribution over the disc contribution. Therefore, we excluded this region and used the time window between 57285 and 58250 for further analysis.

3.3.1 Interpolated cross-correlation analysis

The cross-correlation technique quantifies the degree of similarity between two sets of numbers. The process involves two light curves to assess information between peak/centroid values. One can shift either continuum concerning emission-line light curve or vice versa and calculate the correlation coefficient (r) at each shifted time. Then the peak or the centroid (τ_{cent}) covering $0.8 \times r_{peak}$ is considered as the lag (Peterson et al. 2004). Following Peterson et al. (1998), we performed interpolated cross-correlation function (ICCF).[4] First, the cross-correlation function (CCF) is measured by interpolating the continuum series keeping the emission-line light curve unchanged, and second interpolating the emission-line light curve keeping the continuum light curve unchanged. The final ICCF is determined by averaging these two results. The CCF is characterized by (1) its peak value r_{max}, (2) the time delay corresponding to this value τ_{peak}, and (3) the centroid τ_{cent} of the CCF. The Monte Carlo method of flux randomization (FR) and random subset selection (RSS) is used to estimate the uncertainty in the lag (Peterson et al. 1998, 2004).

We have performed the auto-correlation (ACF) between the two continuum light curves, the 5100 Å and photometric V-band in Fig. 4. The ACF shows a lag of zero-day as expected. We also estimated the time lag between photometric V-band flux versus Hβ and Hγ. ICCF shows a strong peak around 80 d for Hβ and Hγ, and a minor peak at $\sim$180 d that could be due to the seasonal gaps (see discussion in Section 4.1). Therefore, we restricted our analysis to 150 d covering the major peak and estimated lag within that. The ICCF method provides lags between V-band versus Hβ of $79.0^{+7.1}_{-5.0}$ d and between V-band and Hγ of $71.8^{+10.9}_{-18.1}$ d in the observer frame. We obtained a shorter lag for Hγ compared to Hβ, which agrees with the previous studies on different objects (e.g. Bentz et al. 2010).

3.3.2 JAVELIN

We have also used JAVELIN[5] developed by Zu, Kochanek & Peterson (2011) and Zu et al. (2013), which estimates lag by modelling the continuum and line light curves. According to Kelly, Bechtold & Siemiginowska (2009), quasar variability can be well-described by a damped random walk (DRW) process. JAVELIN models the continuum light curve using a DRW having two parameters: amplitude and time-scale of variability. Then the emission line light curve is generated, which is a shifted, scaled, and smoothed version of the continuum light curve. It interpolates between data points and self-consistently estimates and includes the uncertainties in the interpolation. Error estimation uses the Markov Chain Monte Carlo approach to calculate the statistical confidence limits on each best-fitting parameter and

---

[4]https://bitbucket.org/cgrier/python_ccf_code/src/master/
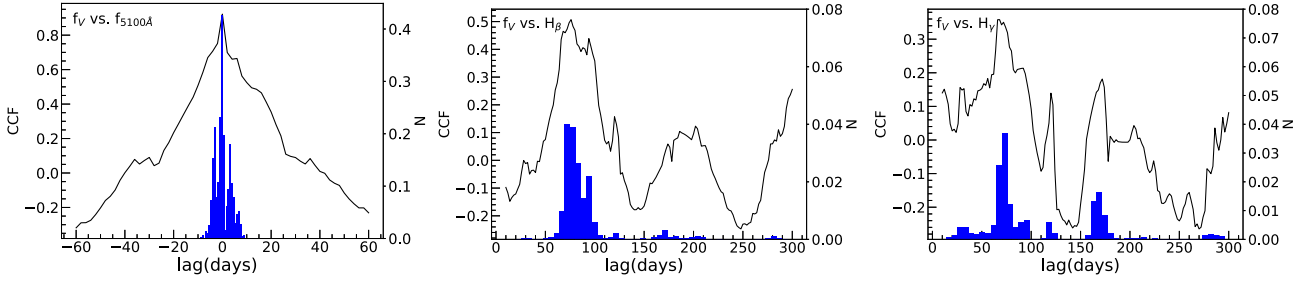[5]https://github.com/nye17/JAVELIN

Figure 4. Cross-correlation function and lag distribution for V-band versus f_{5100} (left), Hβ (middle), and Hγ (right). The ICCF (line) and centroid probability distribution from ICCF (filled histogram) are shown.
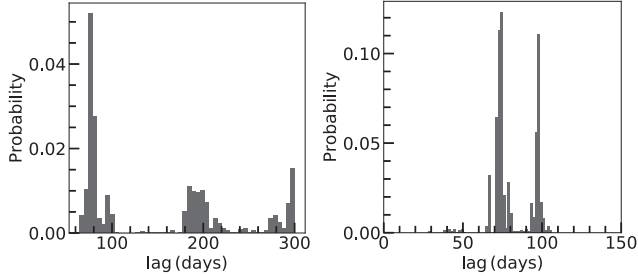

Figure 5. Probability distribution of observed frame lag computed by JAVELIN between V-band versus Hβ (left) and Hγ (right).

Table 4. Columns as follows: (1) method used to calculate the lag(days), (2) depicts lag in observed frame between photometric V-Band versus Hβ, and (3) lag in observed frame between photometric V-Band versus Hγ.

Method	Lag (days)	
	V versus Hβ	V versus Hγ
ICCF	$79.0^{+7.1}_{-5.0}$	$71.8^{+10.9}_{-18.1}$
JAVELIN	$78.2^{+6.8}_{-3.5}$	$74.7^{+22.7}_{-2.8}$
von Neumann	$67.6^{+37.6}_{-31.4}$	$60.0^{+33.5}_{-31.6}$
Bartels	$73.7^{+37.5}_{-28.3}$	$62.2^{+31.4}_{-31.1}$

accurately model the continuum and emission-line light curve simultaneously.

In Fig. 5, the probability distribution of the observed frame lag is plotted, as computed by JAVELIN. The left-hand panel of the figure shows the probability distribution of JAVELIN lag between the V-band light curve versus Hβ; here, too, we noticed a significant peak at $\sim$80 d and multiple minor peaks. Therefore, we calculated a lag between 0 and 150 d, similar to ICCF. We also plotted the probability distribution of lag between the V-band light curve versus Hγ in the right-hand panel for the lag range of 0–150 d. The plots show prominent peaks at $\sim$78 and 75 d for Hβ and Hγ, respectively. These results are consistent with the ICCF. Time delays obtained from JAVELIN are given in Table 4.

3.3.3 The von Neumann and Bartels estimators

This method is based on a mean-square successive-difference estimator (see von Neumann 1941) that handles sparsely and irregularly sampled data and is relevant for the process underlying the variability that cannot be adequately modelled. It does not rely on data interpolation, binning in correlation space, ergodicity arguments,
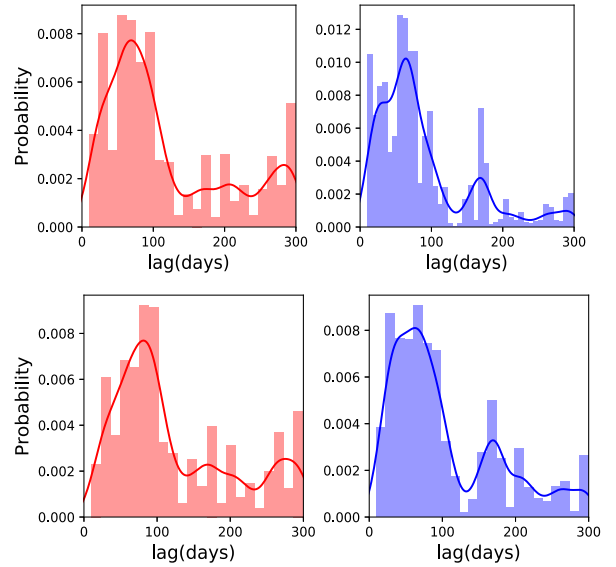

Figure 6. Probability distribution of the observed frame time lag based on the von Neumann estimator (top panels) and the Bartels estimator (bottom panels) for Hβ (left) and Hγ (right).

and stochastic models for quasar variability. Hence, time delay measurements are restricted to the information embedded in the light curves being processed (Chelouche, Pozo-Nuñez & Zucker 2017).

The time delay distribution obtained from the von Neumann method after a Monte Carlo simulation of FR-RSS, as done for the CCF analysis, is shown in the upper panels of Fig. 6. The Hβ and Hγ show firm peaks at $\sim$68 and 60 d, respectively. The Bartels estimator is the modified method of the von Neumann estimator (Bartels 1982), which uses a ranked light curve instead of a sorted one, which can also be used to measure time delay based on the regularity or randomness of data. The lag results are given in Table 4 between time interval taken from 0 to 300 d. The results obtained using von Neumann and Bartels methods are consistent with the lags obtained using ICCF and JAVELIN.

The above methods suggest a time lag of $\sim$80 d between the photometric V-band continuum and the Hβ line light curve. We visually analyse the consistency of the measured lag; the V-band flux light curve along with the Hβ light curve back-shifted by 80 d are plotted in Fig. 7. The continuum and back-shifted line light curves agreeably match. Therefore, we considered the lag of $79.0^{+7.1}_{-5.0}$ d in the observed frame obtained by the ICCF method as the best lag measurement for PKS 0736 + 017.
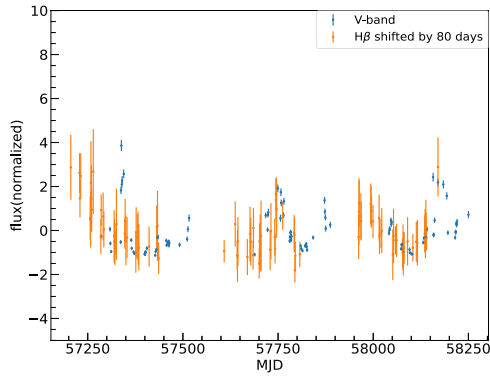
Figure 7. Normalized V-band light curve plotted along with the Hβ light curve back-shifted by 80 d.

3.3.4 Mean and RMS spectra

We constructed mean spectrum and rms spectrum as follows.

$$F\bar{(\lambda)} = \frac{1}{N} \sum_{i=0}^{N-1} F_i(\lambda), \tag{3}$$

and

$$S(\lambda) = \sqrt{\left[\frac{1}{N-1} \sum_{i=0}^{N-1} (F_i(\lambda) - F\bar{(\lambda)}^2) \right]} \tag{4}$$

where $F_i(\lambda)$ is the ith spectrum of the N(127) spectra that comprise the data base. The mean spectrum is the average spectrum of all the spectra obtained during the campaign, whereas the rms spectrum is based on the variation around this mean. The rms spectrum isolates the constant features such as narrow emission line and the host galaxy contribution of the spectrum and hinders accurate line-width measurements. However, the rms spectrum is often too noisy therefore measuring the line width from the rms spectrum is challenging.

In Fig. 8, we showed the mean and rms spectra constructed from all the flux-calibrated spectrum without subtracting from the fitted continuum. The lower panel depicting the rms spectra with and without subtraction from fitted power-law continuum. Both the mean and rms spectra show the presence of strong Balmer lines. Most importantly, the narrow [O III]5007, present in the mean spectrum, disappeared in the rms spectrum suggesting the flux calibration is proper. As noted earlier, although the SO monitoring campaign has used different slits throughout the campaign, the majority of them (107 out of 127) are obtained using 4.1 arcsec slit width. To find out any effect of slit width in the construction of the mean and rms spectra and subsequent analysis, we re-constructed them using only spectra taken with 4.1 arcsec slit. The resultant mean and rms spectra (see Fig. A) is remarkably similar to that obtained using the entire spectral data.

3.3.5 Detection significance of cross-correlation lag

Recent RM studies on large samples perform simulation to access the lag significance (Homayouni et al. 2022; Penton et al. 2022; U et al. 2022), however, there are no universal criteria to define the lag reliability. We used the publicly available PYIICCF code[6] developed
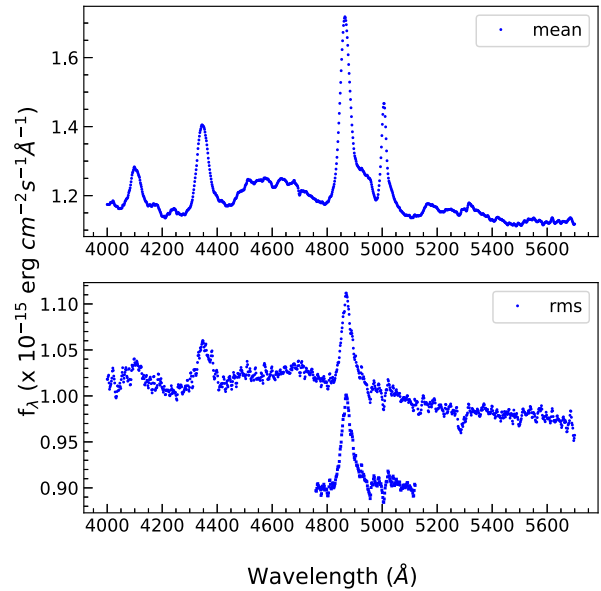
[6]https://github.com/legolason/PyIICCF/

Figure 8. Mean and rms spectra of PKS0736 constructed from the nightly spectrum after rescaling based on [O III]λ5007. Top: mean spectrum. Bottom: rms spectra before (upper plot) and after (lower plot) the continuum subtraction in the region of wavelength window 4760–4790 and 5080–5120 Å.

by Guo, Barth & Wang (2022), which uses the method described in U et al. (2022) to assess the lag significance of our measurement. In this method, two uncorrelated red-noise light curves are simulated with the same S/N and cadence as the observed data to determine the probability of finding the peak of correlation (r_{max}) larger than the observed ICCF peak via null hypothesis test.

For this purpose, we start by simulating the continuum and line light curves using the DRW model. First, we fitted the continuum V-band and Hβ line light curves using the DRW model and used the best-fitting parameters to simulate the corresponding light curves. Secondly, we simulated a 100 times longer light curve than the observed data and randomly selected a portion of the light curve. Thirdly, we added Gaussian noise to the mock light curve based on the uncertainty in the observed light curve. Fourthly, we downsampled the mock light curve to have the same cadence and length as the observed light curve. We simulated 1000 such sets of continuum and line light curves. Finally, we cross-correlated mock continuum light curve with the observed line light curve and vice versa within a lag search range of 0–300 d. From these CCF, we obtained a distribution of τ_{cent} and r_{max} (see Fig. 9). Then we derived the p(r_{max}), which is the ratio of the number of positive lag, with r_{max} larger than the observed r_{max} and $\tau_{cent} > 0$ to the total number of positive lag. This p(r_{max}) provides a way to access the robustness of our lag estimation, a smaller p(r_{max}) gives more robust and reliable lag detection. We found p(r_{max}) is 0.05, which is <0.2 adopted by U et al. (2022) as the limiting condition for reliable lag determination. This suggests that our lag measurement is robust and reliable.

3.3.6 Line width and black hole mass measurement

To estimate the black hole masses, we measured the full width at half-maximum (FWHM) and the line dispersion (σ_{line}) of the Hβ emission line from both the mean and rms spectra after fitting the continuum and subtracting with the same. The FWHM is calculated by finding $0.5 \times F(\lambda)_{max}$ both from the left-hand (λ_l) and right-hand side (λ_r) of the curve and subtracting the two wavelengths i.e, $\lambda_r -$
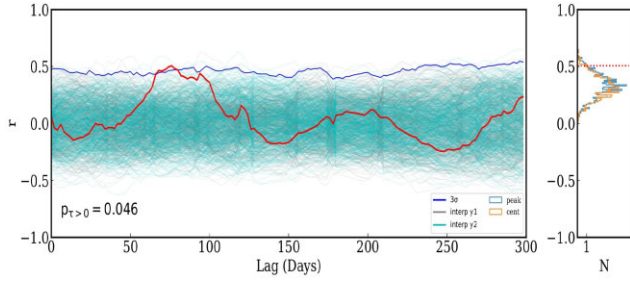
Figure 9. Left: the plot shows the CCF coefficient(r) Vs. lag between V-band continuum and H β line light curve taken in 0–300 d, for all 1000 simulations and the red curve shows the r versus lag for the observed light curves with 3σ confidence interval. Right: CCF peak and centroid distribution of the coefficient and the number of simulations showing r > 0.5.

Table 5. Rest-frame resolution uncorrected line width and black hole mass measurements from mean and rms spectra.

Spectrum	Type	ΔV(km s^{-1})	M_{BH}($\times 10^7$ M$_\odot$)
Mean	FWHM	$2160.14^{+198.65}_{-210.48}$	$6.78^{+1.30}_{-1.26}$
	σ_{line}	$1230.92^{+79.46}_{-74.03}$	$8.78^{+1.17}_{-1.02}$
RMS	FWHM	$1946.48^{+284.58}_{-257.41}$	$5.50^{+1.72}_{-1.36}$
	σ_{line}	$1123.04^{+66.58}_{-72.48}$	$7.32^{+0.89}_{-0.91}$

Columns: Spectrum, line width type, line width, and black hole mass.

λ_l (Peterson et al. 2004). Whereas, for the calculation of σ_{line}, the flux weighted line centre was first determined as follows:

$$\lambda_0 = \frac{\int \lambda f_\lambda \, d\lambda}{\int f_\lambda \, d\lambda} \quad (5)$$

and the line dispersion is

$$\sigma_{line}^2 = \frac{\int \lambda^2 f_\lambda \, d\lambda}{\int f_\lambda \, d\lambda} - \lambda_0^2 \quad (6)$$

The values are mentioned in Table 5. The same for spectra taken with 4.1 arcsec slit is given in Table A1, which shows consistent results justifying the line-width measurements from the entire spectral data.

Assuming that the black hole's gravitational potential governs the gas motion in the BLR, black hole mass can be estimated by combining the size of the BLR (R_{BLR}) and the velocity width of broad emission lines (ΔV) based on the virial relation:

$$M_{BH} = \frac{f \times R_{BLR}(\Delta V)^2}{G} \quad (7)$$

where f is a dimensionless scale factor that depends on the kinematics and geometry of BLR gas clouds. The BLR size (calculated from time lag $R_{BLR} = c\tau$) and line width (from mean and rms spectra) with f of 4.47(σ) or 1.12 (FWHM), taken from (Woo et al. 2015), is used to calculate black hole mass. The Monte Carlo bootstrap method (Peterson et al. 2004) was used to estimate uncertainty in the line-width measurements and hence the black hole mass. N spectra were chosen randomly from a set of N spectra without replacement for each realization, and line width was measured from the mean and rms spectra. We varied the end points randomly within ± 10 Å of the initially selected H β region (i.e. 4800–4920 Å). Finally, a total of 5000 realizations were performed, providing a distribution of FWHM and σ_{line}. The mean of the distribution is the final line width, and the standard deviation of the distribution (34 percentile of both sides of the mean i.e. the 16th and the 84th percentiles of the distribution) was considered the measurement uncertainty. The

resultant line-width measurement along with black hole mass is given in Table 5.

Using the cross-correlation method, we obtained a lag (τ_{cent}) between optical V-band and H β (H γ) of $66.4^{+6.0}_{-4.2}$ ($60.4^{+9.2}_{-15.3}$) d in rest frame. We used the virial relation with f of 4.47(1.12) for σ_{line}(FWHM), providing four different black hole masses based on the four different choices of line widths. We note that σ_{line} is less sensitive to the line peak and that FWHM is less sensitive to the line wing; therefore, black hole masses based on the σ_{line} are widely adopted as the best mass measurement (e.g. Peterson et al. 2004, 2014). Therefore, a black hole mass of $7.32^{+0.89}_{-0.91} \times 10^7 M_\odot$ from the σ_{line} of the rms spectrum is found for PKS0736.

4 DISCUSSION

4.1 Effect of seasonal gaps on lag estimate

Due to the low declination, the monitoring observations of PKS0736 are affected by the seasonal gaps, as can be seen from the light-curve plot. We have simulated light curves to investigate the impact of seasonal gaps on the lag measurement. We have constructed a mock continuum light curve using the DRW model of JAVELIN having the same properties (i.e. same amplitude and time-scale of variation) as the observed V-band continuum light curve. Then, we simulated the emission-line light curve from the mock continuum light curve with a shift of 80 d based on our calculated lag from the observed data, smoothing and scaling the mock light curve to mimic the observed light curve. We then downsampled the light curves to have the same observational gaps.

We then performed all the time-series analysis methods to recover the time lag of 80 d from the simulated data. The results are shown in Fig. B1 and tabulated in Table B1 for a single set of mock light curves. We noticed a strong peak at ~80 d in all the methods, i.e. ICCF, JAVELIN, von Neumann, and Bartels, which well-recovered the input lag, suggesting the observed cadence and seasonal gaps do not affect our lag estimation. Although a secondary peak of around 180 d has been seen from CCF and JAVELIN, it is well-separated from the primary peak and does not affect our lag measurements. Moreover, the peak of the ICCF ($r_{max} \sim 0.5$) matches well with that obtained from the observed data (see middle panel of Fig. 4). We further simulated such 500 sets of continuum and line light curves and repeated the above process of measuring lag. In Fig. B2, we showed the distribution of lag ratio recovered from the ICCF to the input lag of 80 d, which provides a ratio of unity. Based on these simulations, we conclude a H β lag of ~80 d from the observed data of PKS0736.

4.2 Size–luminosity relation

The PKS0736 is a radio-loud AGN having a combination of thermal emission from the disc and non-thermal emission from the jet elucidated by Fig. 3. Consequently, the measurement of L_{5100} is affected by non-thermal emission. However, we considered the quiescent state by removing the flaring region as visible in the γ-ray light curve (Fig. 2).

We plotted PKS0736 in the size–luminosity diagram as shown in Fig. 10 along with various objects from the literature. The PKS0736 follows the best-fitting size–luminosity relation given by Bentz et al. (2013). Hence, its position is found to be consistent with the size−luminosity relation of other AGN. Du & Wang (2019) has provided a new scaling relation, taking into account the Fe II emission contamination in the spectrum of quasars and for especially high
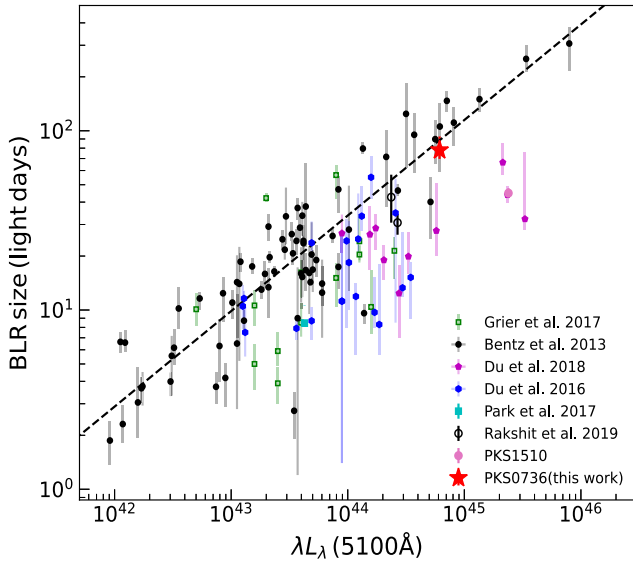
Figure 10. The plot is between the BLR size versus L_{5100} relation of AGNs. The source PKS0736 is following the relation very well. The best-fitting relation of Bentz et al. (2013) is shown along with various RM results from the literature.

accreting AGN. This new scaling relation can explain the deviation seen in high-accreting sources from the size–luminosity relation. We estimate Fe II strength from the continuum-subtracted mean spectrum. The strength of Fe II ($R_{Fe\,II}$), which is the flux ratio of Fe II (4435–4685 Å) to H β is found to be 0.58 ± 0.08. Therefore, PKS0736 is a moderately strong Fe II emitter. The time-lag estimated using scaling relation of Du & Wang (2019) is around 63 light-days, which is slightly lower than the 87 light-days estimated using Bentz et al. (2013).

The disc luminosity of PKS0736 was measured by several authors and found to be in the range of $10^{44.6}$–$10^{45.7}$ ergs s^{-1} (see McLure & Dunlop 2001; Dai et al. 2007; Abdalla et al. 2020). The scaling relation $R_{BLR} = 10^{17} \sqrt{L_{disk}/10^{45}}$cm (Ghisellini & Tavecchio 2009) provides R_{BLR} = 24–86 light-days, our measured BLR size of 66 light-days is within this range. Alternatively, the NTD in the quiescent state can be used as an estimator for removing non-thermal contribution from the observed L_{5100}. The median of NTD which is measured as $2.51^{+1.52}_{-0.65}$ indicates ∼ 33 per cent of disc contribution in L_{5100}. If we use this revised L_{5100} value of 1.44×10^{44}, the expected BLR size based on Bentz et al. (2013) is found to be 41 light-days, which is slightly smaller than our estimated rest frame BLR size of 66 light-days.

We have also performed the ICCF analysis between radio (see Fig. 2) and V-band light curves. The correlation between radio and optical is found to be very weak with $r_{max} \sim 0.3$. The measured lag is ∼255 light-days which is much longer than the lag of H β. The weak correlation between radio and optical and a much longer radio lag than H β lag suggest the radio-emitting region is different than the H β emitting region and radio is not the primary contributor in the V-band fluxes within the time-range studied.

4.3 The effect of diffuse continuum

Continuum RM study of AGNs showed the UV-optical lags generally follow the $\tau \propto \lambda^{4/3}$ in agreement with the simple irradiated disc models; however, larger by a factor of 2–4 than predicated by standard accretion disc (see e.g. Fausnaugh et al. 2016; Edelson et al. 2019;

Guo et al. 2022, and references therein). Diffuse continuum (DC) emission from the BLR has been suggested as the possible origin of this larger-than-expected lag (Korista & Goad 2001; Lawther et al. 2018; Chelouche, Pozo Nuñez & Kaspi 2019; Korista & Goad 2019). Recently, Netzer (2022) showed that time-dependent emission of the diffuse BLR gas could explain the observed large lag in the continuum RM. The DC could affect our NTD calculation and the BLR size–luminosity relation. Assuming the radiation pressure-confined cloud models and a covering factor of 0.2, the Netzer (2022) showed that the DC fraction could be 23 per cent of the total continuum at 5100 Å for a source with $L_{total,\,5100} = L_{disc,\,5100} + L_{DC,\,5100} = 10^{44}$ erg s^{-1}. The DC has two effects on the BLR size–luminosity relation. First, the true $L_{disc,\,5100}$ will be lower than the observed $L_{total,\,5100}$ and this will reduce the expected BLR size by 12 per cent (∼4 d) for a source with $L_{total,\,5100} = 10^{44}$ erg s^{-1} (see their equation 3). The NTD values are calculated based on the observed to predicted luminosity ratio. The $L_{5100,\,disc}$ should be lower if DC is taken into account; however, the predicted luminosity will also be affected as the correlation between L(H β) versus $L_{total,\,5100}$ for the SDSS DR14 quasars is not corrected for DC. Second, since the lag is measured with respect to V-band, the reference point will be shifted towards a higher lag due to DC. Therefore, the true lag should be smaller by a few days, ∼4 d for $L_{total,\,5100} = 10^{44}$ erg s^{-1} (see equation 6 of Netzer 2022). Both the size of the BLR and the luminosity of the continuum will be smaller by a similar extent for all the objects depending on the luminosity. Hence, the size–luminosity relation may not be affected much. A detailed quantitative analysis of this issue is beyond the scope of this paper.

4.4 Black hole mass measurement

Previous studies have estimated a range of black hole masses of PKS0736 from 10^8 to $10^{8.73}$ M$_{\odot}$ (Schmidt et al. 1992; McLure & Dunlop 2001; Marchesini et al. 2004; Dai et al. 2007; Abdalla et al. 2020). These estimates are based on the scaling relationship ($R_{BLR} \propto L_{5100}^{\alpha}$) (e.g. Kaspi et al. 2000) measured from the single-epoch spectrum. Since PKS0736 is highly variable, the measurement of black hole mass from the single-epoch spectrum is highly uncertain. We note that single-epoch mass measurements are affected by choice of line width used to estimate the black hole. Generally, most of the single-epoch masses are calculated using FWHM; however, it has been found from the RM study of AGNs with multiple emission lines that σ_{line} provides a better measure of the black hole mass (Peterson et al. 2004). The rms spectrum isolates the non-varying components (e.g. narrow emission lines, host galaxy) and provides a robust estimation of black hole masses. Our reverberation-based black hole mass is found to be between 5.50 and 8.78 × 10^7 M$_{\odot}$ depending on the line width estimator and type of spectrum. However, we consider the black hole masses of $7.32^{+0.89}_{-0.91} \times 10^7 M_{\odot}$ calculated from the σ_{line} of the rms spectrum as the best black hole mass measurement.

The bolometric luminosity of PKS0736 is calculated as 5.52×10^{45} erg s^{-1}, using mean L_{5100} and the relation $L_{BOL} = 9 \times L_{5100}$ (Kaspi et al. 2000). The Eddington luminosity (L_{EDD}) is estimated as 9.22×10^{45} erg s^{-1}, whereas the Eddington ratio (λ_{EDD}) is 0.60 calculated by $L_{EDD} = 1.26 \times 10^{38} M_{BH}$ and the black hole mass based on the σ_{line} of rms spectrum. This suggests that PKS0736 is accreting at a sub-Eddington rate.

5 CONCLUSIONS

We analysed the SO spectrophotometric data for PKS0736 obtained between 2014 November and 2018 May, rendering more than 100

spectra and photometric data points. We found strong variability in the photometric light curve with $F_{var} = 69.86 \pm 4.30$ per cent, which is also reflected in the spectroscopic continuum with zero lag. Both the Hβ and Hγ show high variability with F_{var} of 21.10 ± 1.79 per cent and 29.73 ± 2.25 per cent, respectively. The estimated NTD is found to be 2.51, suggesting about 67 per cent contribution from the non-thermal emission towards the observed mean L_{5100} of 6.13×10^{44} ergs s^{-1}. Using the cross-correlation method, we obtained a lag between optical V-band and Hβ (Hγ) of $66.4^{+6.0}_{-4.2}$ ($60.4^{+9.2}_{-15.3}$) in the rest frame. Using virial relation and a scale factor of $f = 1.12$ ($f = 4.47$) for FWHM (σ_{line}), a black hole mass of $7.32^{+0.89}_{-0.91} \times 10^7 M_\odot$ is obtained from the rms spectrum and σ_{line} of Hβ line profile. The position of PKS0736 is consistent with the size−luminosity relation of AGNs.

ACKNOWLEDGEMENTS

DATA AVAILABILITY

The data underlying this article were accessed from the Steward Observatory data base with the following link: http://james.as.arizona.edu/~psmith/Fermi/ (see, Smith et al. 2009). The derived data generated in this research are available in the article and in its online supplementary material.

REFERENCES

Abdalla H. et al., 2020, A&A, 633, A162
Abdo A. A. et al., 2009, ApJ, 707, 55
Amaya-Almazán R. A., Chavushyan V., Patiño-Álvarez V. M., 2022, ApJ, 929, 14
Amorim A. et al., 2021, A&A, 654, A85
Bahcall J. N., Kozlovsky B.-Z., Salpeter E. E., Bahcall J. N., Kozlovsky B.-Z., Salpeter E. E., 1972, ApJ, 171, 467
Baldwin J. A., 1975, ApJ, 201, 26
Bartels R., 1982, J. Am. Stat. Assoc., 77, 40
Barth A. J. et al., 2015, ApJS, 217, 26
Bentz M. C. et al., 2009, ApJ, 705, 199
Bentz M. C. et al., 2010, ApJ, 720, L46
Bentz M. C. et al., 2013, ApJ, 767, 149
Bentz M. C., Williams P. R., Treu T., 2022 ApJ, 934, 168
Blandford R. D., McKee C. F., Blandford R. D., McKee C. F., 1982, ApJ, 255, 419
Bloom S., Marscher A., Moore E., Gear W., Teräsranta H., Valtaoja E., Aller H., Aller M., 2009, ApJS, 122, 1
Bontà E. D. et al., 2020, ApJ, 903, 112
Cackett E. M., Bentz M. C., Kara E., 2021, iScience, 24, 102557
Chavushyan V., Patiño-Álvarez V. M., Amaya-Almazán R. A., Carrasco L., 2020, ApJ, 891, 68
Chelouche D., Pozo-Nuñez F., Zucker S., 2017, ApJ, 844, 146
Chelouche D., Pozo Nuñez F., Kaspi S., 2019, Nature Astron., 3, 251
Cho H. et al., 2020, ApJ, 892, 93
Clements S. D., Jenks A., Torres Y., 2003, AJ, 126, 37
Dai H., Xie G. Z., Zhou S. B., Li H. Z., Chen L. E., Ma L., 2007, AJ, 133, 2187
Dehghanian M. et al., 2021, ApJ, 906, 14
Dietrich M. et al., 2012, ApJ, 757, 53
Du P., Wang J.-M., 2019, ApJ, 886, 42
Du P. et al., 2014, ApJ, 782, 45
Du P. et al., 2015, ApJ, 806, 22
Du P. et al., 2016a, ApJ, 820, 27
Du P. et al., 2016b, ApJ, 825, 126
Du P. et al., 2018, ApJ, 856, 6
Edelson R. et al., 2019, ApJ, 870, 123
Falomo R., Ulrich M. H., 2000, A&A, 357, 91
Fausnaugh M. M. et al., 2016, ApJ, 821, 56
Fausnaugh M. M. et al., 2017, ApJ, 840, 97
Fermi Large Area Telescope Collaboratin, 2021, Astron. Telegram, 15110, 1
Fossati G., Maraschi L., Celotti A., Comastri A., Ghisellini G., 1998, MNRAS, 299, 433
Ghisellini G., Tavecchio F., 2009, MNRAS, 397, 985
Gower A. C., Hutchings J. B., Gower A. C., Hutchings J. B., 1984, AJ, 89, 1658
Gravity Collaboration, 2018, Nature, 563, 657
GRAVITY Collaboration et al.2020, A&A, 643, A154
Greene J. E., Ho L. C., 2005, ApJ, 630, 122
Grier C. J. et al., 2012, ApJ, 755, 60
Grier C. J. et al., 2017, ApJ, 851, 21
Guo H., Barth A. J., Wang S., 2022, preprint (arXiv:2207.06432)
Homayouni Y. et al., 2022, ApJ, 926, 225
Impey C. D., Neugebauer G., 1988, AJ, 95, 307
Joly M., 1988, A&A, 192, 87
Kaspi S., Smith P. S., Netzer H., Maoz D., Jannuzi B. T., Giveon U., 2000, ApJ, 533, 631
Kaspi S., Brandt W. N., Maoz D., Netzer H., Schneider D. P., Shemmer O., 2007, ApJ, 659, 997
Kellermann K. I., Vermeulen R. C., Zensus J. A., Cohen M. H., 1998, AJ, 115, 1295
Kelly B. C., Bechtold J., Siemiginowska A., 2009, ApJ, 698, 895
Korista K. T., Goad M. R., 2001, ApJ, 553, 695
Korista K. T., Goad M. R., 2004, ApJ, 606, 749
Korista K. T., Goad M. R., 2019, MNRAS, 489, 5284
Kormendy J., Ho L. C., 2013, ARA&A, 51, 511
Lawther D., Goad M. R., Korista K. T., Ulrich O., Vestergaard M., 2018, MNRAS, 481, 533
Lynds C. R., 1967, ApJ, 147, 837
Malkan M. A., Moore R. L., 1986, ApJ, 300, 216
Mandal A. K., Rakshit S., Stalin C. S. et al., 2020, MNRAS, 501, 3905
Marchesini D., Celotti A., Ferrarese L., 2004, MNRAS, 351, 733
McLure R. J., Dunlop J. S., 2001, MNRAS, 327, 199
McLure R. J., Kukula M. J., Dunlop J. S., Baum S. A., O'Dea C. P., Hughes D. H., 1999, MNRAS, 308, 377
Nalewajko K., Gupta A. C., Liao M., Hryniewicz K., Gupta M., Gu M., 2019, A&A, 631, A4
Netzer H., 2022, MNRAS, 509, 2637
Pancoast A., Brewer B. J., Treu T. et al., 2014, MNRAS, 445, 3073
Park S. et al., 2017, ApJ, 847, 125
Pei L. et al., 2017, ApJ, 837, 131
Penton A. et al., 2022, MNRAS, 509, 4008
Peterson B. M., 1993, PASP, 105, 247
Peterson B. M., 2014, Space Sci. Rev., 183, 253
Peterson B. M., Wanders I., Bertram R., Hunley J. F., Pogge R. W., Wagner R. M., 1998, ApJ, 501, 82
Peterson B. M. et al., 2002, ApJ, 581, 197
Peterson B. M. et al., 2004, ApJ, 613, 682

Peterson B. M. et al., 2014, ApJ, 795, 149
Rakshit S., 2020, A&A, 642, A59
Rakshit S., Woo J.-H., Gallo E. et al., 2019, ApJ, 886, 93
Rakshit S., Stalin C. S., Kotilainen J., 2020, ApJS, 249, 17
Richards J. L. et al., 2011, ApJS, 194, 29
Rodriguez-Pascual P. M. et al., 1997, ApJS, 110, 9
Romney J. et al., 1984, A&A, 135, 289
Schmidt G. D., Stockman H. S., Smith P. S., 1992, ApJ, 398, L57
Shaw M. S. et al., 2012, ApJ, 748, 49
Shen Y. et al., 2016, ApJ, 818, 30
Smith P. S., Montiel E., Rightley S., Turner J., Schmidt G. D., Jannuzi B. T., 2009, preprint (arXiv:0912.3621)
Tadhunter C. N., Morganti R., di Serego Alighieri S., Fosbury R. A. E., Danziger I. J., 1993, MNRAS, 263, 999
U V. et al., 2022, ApJ, 925, 52
Ulrich M.-H., Maraschi L., Urry C. M., 1997, ARA&A, 35, 445
Urry C. M., Padovani P., 1995, PASP, 107, 803
Villafaña L. et al., 2022, ApJ, 930, 52
von Neumann J., 1941, Ann. Math. Stat., 12, 367
Wagner S. J., Witzel A., 1995, ARA&A, 33, 163
Wandel A., Peterson B. M., Malkan M. A., 1999, ApJ, 526, 579
Williams P. R. et al., 2020, ApJ, 902, 74
Woo J. H., Yoon Y., Park S., Park D., Kim S. C., 2015, ApJ, 801, 1
Woo J.-H., Urry C. M., 2002, ApJ, 579, 530
Wright S. C., McHardy I. M., Abraham R. G., 1998, MNRAS, 295, 799
Zajaček M. et al., 2020, ApJ, 896, 146
Zhang Z.-X. et al., 2019, ApJ, 876, 49
Zu Y., Kochanek C. S., Peterson B. M., 2011, ApJ, 735, 80
Zu Y., Kochanek C. S., Kozłowski S., Udalski A., 2013, ApJ, 765, 106

SUPPORTING INFORMATION

Supplementary data are available at *MNRAS* online.

suppl_data

Please note: Oxford University Press is not responsible for the content or functionality of any supporting materials supplied by the authors. Any queries (other than missing material) should be directed to the corresponding author for the article.

APPENDIX A: ANALYSIS OF TOTAL 107 SPECTRA TAKEN WITH 4.1 ARCSEC SLIT

Although monitoring observations were carried out using multiple slits, the majority of them (84 per cent spectra) are taken with 4.1 arcsec slit width. To investigate whether the different slit widths used during spectroscopic observations of PKS0736 have any effect on the line width measurement and subsequently the black hole mass estimation, we constructed the mean and rms spectra only with the 107 spectra taken with 4.1 arcsec slit width. Fig. A1 is remarkably similar to the mean and rms spectra obtained from entire spectroscopic data (see Fig. 8) provided from SO irrespective of the slit width used during observation. Moreover, we estimated FWHM and σ from these mean and rms spectra. The results are given in Table A1, which shows consistent results that obtained with entire spectroscopic data (see Table 5). It suggests that the use of entire spectral data do not affect black hole mass measurement.
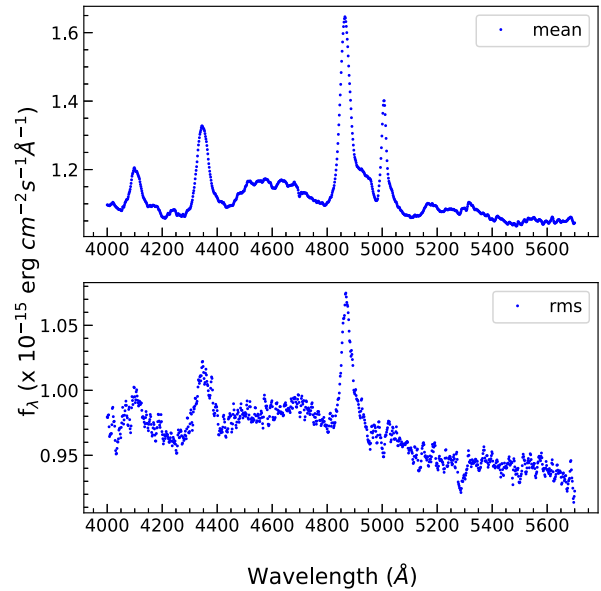

Figure A1. Mean and RMS spectra of PKS0736 from the 107 spectra obtained using 4.1 arcsec slit after rescaling based on [O III]λ5007 without continuum subtracted from nightly spectra.

Table A1. Rest-frame resolution uncorrected line width and black hole mass measurements from mean and rms spectra.

Spectrum	Type	$\Delta V (\mathrm{km\,s^{-1}})$	$M_{BH}(\times\,10^7\,M_\odot)$
Mean	FWHM	$2147.08^{+196.95}_{-222.35}$	$6.60^{+1.26}_{-1.29}$
	σ_{line}	$1223.05^{+82.62}_{-73.72}$	$8.55^{+1.19}_{-1.00}$
RMS	FWHM	$1934.60^{+257.63}_{-258.21}$	$5.36^{+1.52}_{-1.33}$
	σ_{line}	$1064.81^{+80.42}_{-79.15}$	$6.48^{+1.01}_{-0.92}$

Columns: Spectrum, line width type, line width, and black hole mass. 629

APPENDIX B: TIME-SERIES ANALYSIS OF SIMULATED LIGHT CURVES

We have performed time-series analysis on the simulated data as mentioned in Section 4.1. The results of the time-series analysis are shown in Fig. B1 for ICCF, JAVELIN, Von-Neumann, and Bartels. Table B1 summarizes the results.

Table B1. Columns as follows: (1) the method used to calculate the lag (days) and (2) lag recovered from the simulated light curves with an input lag of 80 d.

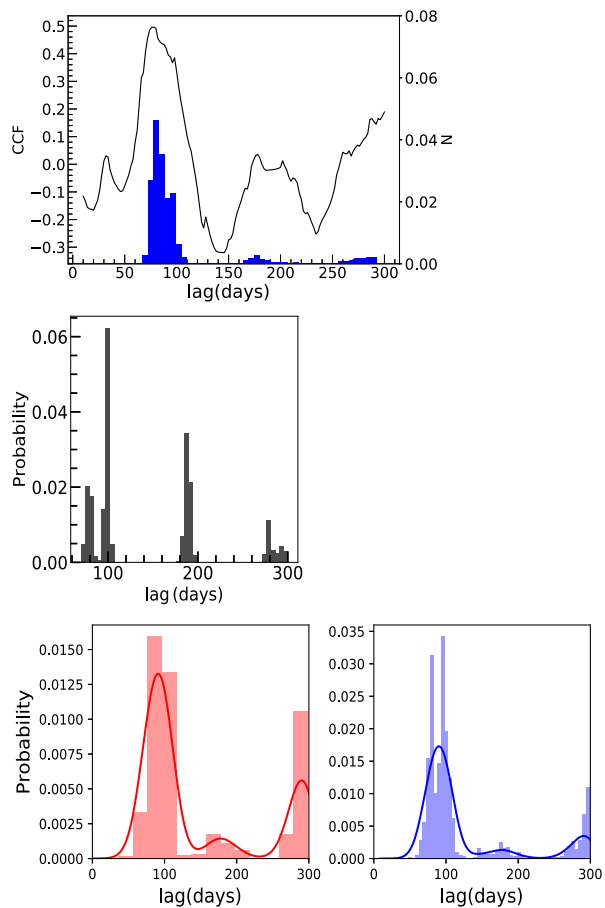| Method	Lag (d)
ICCF	$84.0^{+7.1}_{-11.0}$
JAVELIN	$97.7^{+2.8}_{-17.7}$
von Neumann	$90.4^{+13.4}_{-13.1}$
Bartels	$90.5^{+12.6}_{-11.5}$

Figure B1. Lag estimation from the simulated light curves. Top: cross-correlation function and lag distribution for simulated data. The ICCF (line) and centroid probability distribution from ICCF (filled histogram) are shown. Middle: lag probability distribution obtained from JAVELIN for simulated data. Bottom: lag probability distribution obtained from Von-Neumann (left) and Bartels (right) for simulated data.
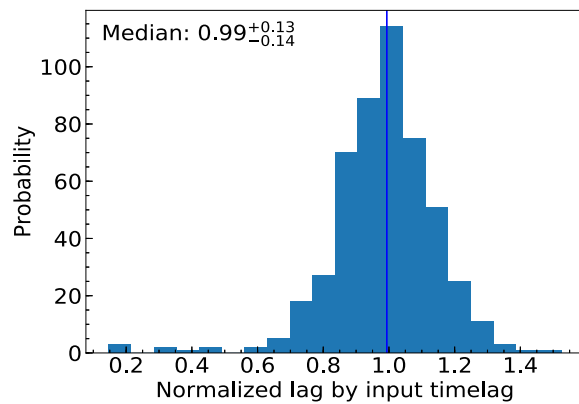
Figure B2. We simulated the light curves for both photometric V-band flux and H β flux over 500 times and plotted the distribution of the ratio of the output lag to input lag (80 d). The median of the histogram, which is closer to value 1, suggests the estimated lag is reliable.

This paper has been typeset from a TEX/LATEX file prepared by the author.